Coastal polynyas enable transitions between high and low West Antarctic ice shelf melt rates
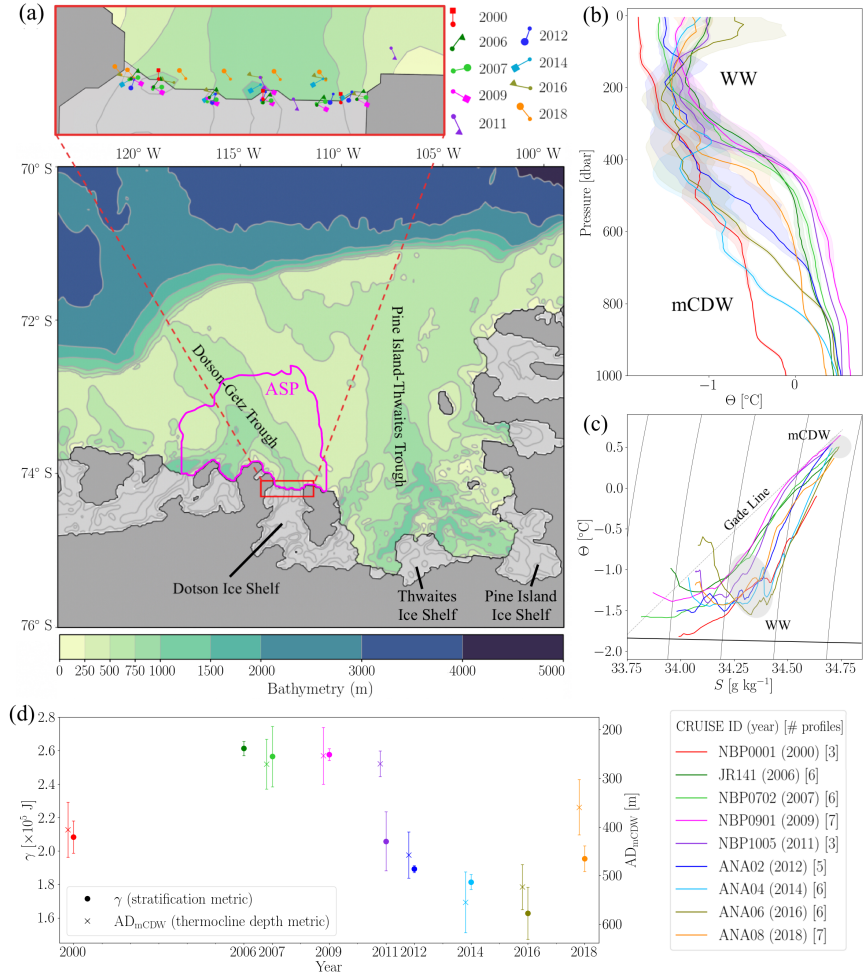
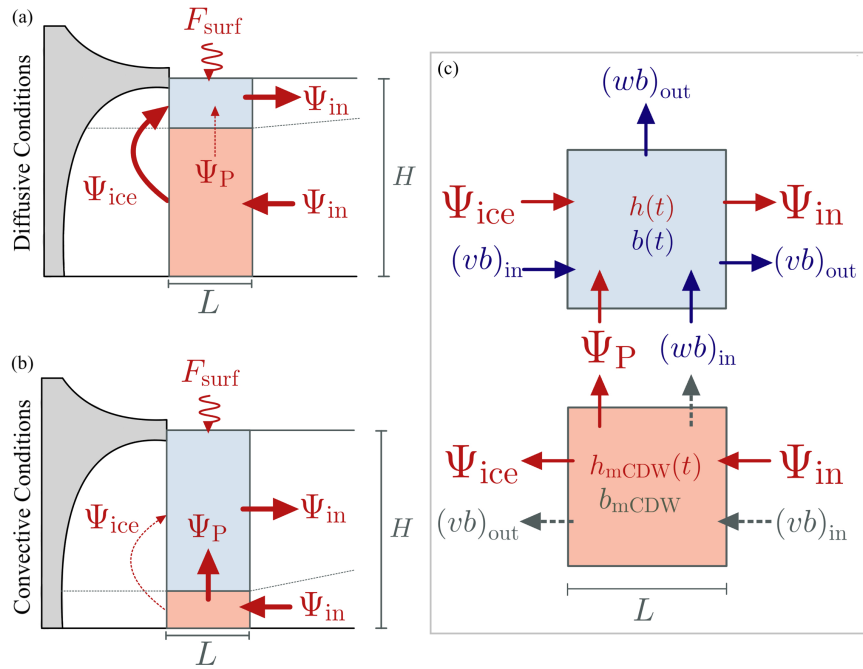Ruth Moorman[1], Andrew F. Thompson[1], and Earle Andre Wilson[1]
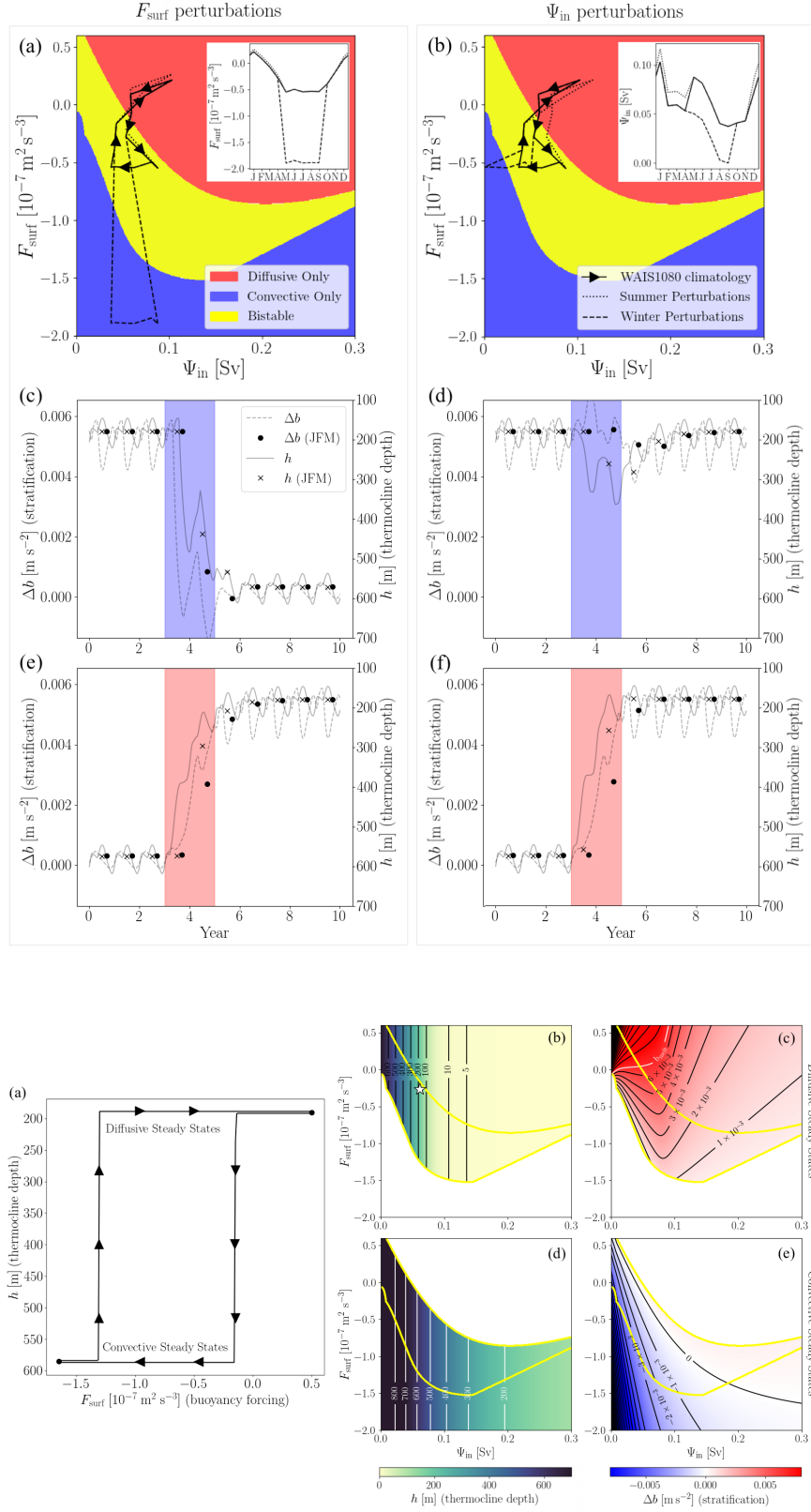
[1]California Institute of Technology

June 1, 2023

Abstract

Melt rates of West Antarctic ice shelves in the Amundsen Sea track large decadal variations in the volume of warm water at their outlets. This variability is generally attributed to wind-driven variations in warm water transport towards ice shelves. Inspired by conceptual representations of the global overturning circulation, we introduce a simple model for the evolution of the thermocline, which caps the water warm layer at the ice-shelf front. This model demonstrates that interannual variations in coastal polynya buoyancy forcing can generate large decadal-scale thermocline depth variations, even when the supply of warm water from the shelf-break is fixed. The modeled variability involves transitions between bistable high and low melt regimes, enabled by feedbacks between basal melt rates and ice front stratification strength. Our simple model captures observed variations in near-coast thermocline depth and stratification strength, and poses an alternative mechanism for warm water volume changes to wind-driven theories.

Coastal polynyas enable transitions between high and low West Antarctic ice shelf melt rates

Ruth Moorman[1], Andrew F. Thompson[1], and Earle A. Wilson[2]

[1]Environmental Science and Engineering, California Institute of Technology, Pasadena, California, USA
[2]Department of Earth System Science, Stanford University, Stanford, California, USA

Key Points:

- Rates of ocean-driven Amundsen Sea ice shelf melt respond to variations in warm water transport to the coast and modification at the coast.
- A simple Amundsen Sea continental shelf overturning model, based on water mass transformation, reveals bistable high and low melt regimes.
- Feedbacks between glacial melt and polynya convection are central to the bistability and produce variability consistent with observations.

Corresponding author: Ruth Moorman, `rmoorman@caltech.edu`

Abstract

Melt rates of West Antarctic ice shelves in the Amundsen Sea track large decadal variations in the volume of warm water at their outlets. This variability is generally attributed to wind-driven variations in warm water transport towards ice shelves. Inspired by conceptual representations of the global overturning circulation, we introduce a simple model for the evolution of the thermocline, which caps the water warm layer at the ice-shelf front. This model demonstrates that interannual variations in coastal polynya buoyancy forcing can generate large decadal-scale thermocline depth variations, even when the supply of warm water from the shelf-break is fixed. The modeled variability involves transitions between bistable high and low melt regimes, enabled by feedbacks between basal melt rates and ice front stratification strength. Our simple model captures observed variations in near-coast thermocline depth and stratification strength, and poses an alternative mechanism for warm water volume changes to wind-driven theories.

Plain Language Summary

Ice loss from the West Antarctic Ice Sheet contributes significantly to current rates of global sea-level rise and threatens to raise sea-levels by 5 m should it collapse completely. The ice sheet is primarily losing mass via glaciers that flow from the Antarctic continent into the Amundsen Sea, where floating ice shelves are exposed to much warmer ocean waters than elsewhere around Antarctica. In this work we present a simplified mathematical model for the volume of warm water at Amundsen Sea ice shelf fronts that successfully reproduces observed patterns of warm water variability. The modeled variability relies on interactions between ice shelf melt and coastal polynyas, regions where enhanced wintertime sea-ice production can trigger mixing that diverts heat carried by warm waters away from the ice shelf and into the atmosphere. Higher melt rates inhibit polynya convection, allowing more warm water to access the ice shelf cavity and reinforcing a high melt state, whilst lower melt rates facilitate polynya convection, diverting heat away from the ice shelf and reinforcing a low melt state. Our results promote the importance of coastal processes in explaining observed variations in Amundsen Sea ice shelf melt, which have previously been attributed to remote wind patterns.

1 Introduction

Recorded mass loss from the West Antarctic Ice Sheet (WAIS) has been driven by the accelerating flow of ice streams that terminate at rapidly thinning ice shelves in the Amundsen Sea embayment (Mouginot et al., 2014; Paolo et al., 2015; IMBIE Team, 2018). These ice streams drain a land ice catchment containing a potential ∼1.2 m of sea level rise (Fretwell et al., 2013). Whilst ice shelf thinning does not directly impact the ice sheet mass balance, the restraining or "buttressing" effect of floating ice shelves on upstream grounded ice flow is critical for limiting ice discharge through glaciers (Fürst et al., 2016; Morlighem et al., 2020). The observed thinning of buttressing ice shelves in the Amundsen Sea has been associated with high rates of basal melt driven by modified Circumpolar Deep Water (mCDW) (Adusumilli et al., 2020; Pritchard et al., 2012; Shepherd et al., 2004; Turner et al., 2017); a warm (2-4°C above freezing) water mass that floods the lower layers of the West Antarctic continental shelf and carries heat from the open ocean to ice shelf cavities via glacially-carved troughs (Walker et al., 2007; Dutrieux et al., 2014). Future projections of the WAIS require accurate representation of forcings that dictate the access of warm mCDW to Amundsen Sea ice shelf cavities.

Hydrographic observations from the Amundsen Sea embayment reveal decadal variations in the thickness of the mCDW layer (Dutrieux et al., 2014; Jenkins et al., 2018) that overwhelm multidecadal ocean warming trends previously considered the driver of ice shelf thinning (Schmidtko et al., 2014). This decadal variability is well observed in front of the Dotson Ice Shelf (Figure 1a), a rapidly thinning shelf buttressing the Kohler

and Smith glaciers (Paolo et al., 2015). Here, the Amundsen Sea Polynya (ASP) permits the repeated collection of summertime hydrographic profiles along the ice shelf front between 2000 and 2018 (Figure 1). These observations reveal high amplitude (~ 400 m), low frequency (~ 10 year period) variability in the thermocline depth, characterized by a warm phase with thick mCDW from 2006-2011 followed by a cool phase with thin mCDW from 2012-2016 and a potential return to warm conditions in 2018 (Figure 1b,d) (Jenkins et al., 2018; Kim et al., 2021). The observed thermocline variability has been linked to Dotson Ice Shelf basal melt rates (Jenkins et al., 2018) and may be implicated in ice shelf thinning trends, either via historical warm phases triggering geometric grounding line retreat that continues to the present (Jenkins et al., 2016) or via a trend in the frequency of warm phases unresolved by the short observational record (Naughten et al., 2022).

Though past studies have shown correlations between shoreward mCDW transport and wind forcing over the shelf-break, the mechanistic link between these processes remains uncertain. Studies focused on monthly to interannual timescales suggest eastward wind anomalies over the shelf enhance mCDW transport through troughs via barotropic acceleration of the Amundsen undercurrent (Assmann et al., 2013; Dotto et al., 2019, 2020; Naughten et al., 2022) and localized shelf-break (Kim et al., 2017; Webber et al., 2019) or shelf integrated (Kim et al., 2021) Ekman pumping. By contrast, Silvano et al. (2022) find the opposite relation at decadal timescales, an anticorrelation between eastward wind anomalies and shoreward mCDW transport, due to baroclinic adjustment of the Amundsen undercurrent. Though proposed mechanisms differ, these studies consistently present wind-driven variability of shoreward mCDW transport as the driver of decadal thermocline depth variability and related melt variability in the Amundsen sector.

There are indications that the wind-driven framework is incomplete. Coastal thermocline depth and heat content variability is substantially amplified relative to the shelf-break in both observations and simulations (e.g. Kim et al., 2021; Silvano et al., 2022; Naughten et al., 2022), a feature not yet explained by wind-driven mechanisms. Further, while thermocline displacements predicted from winds correlate well with observations, they underestimate the amplitude of coastal signals (Kim et al., 2021). Prompted by this amplitude gap, we revisit the Dotson Ice Front hydrography. Years with thick mCDW layers (2006-2011) are consistently associated with stronger stratification (Figure 1d) and more buoyant, meltwater modified Winter Waters (WW) relative to years with thin mCDW layers (2000, 2012-2016). Further, during warm years, modification by glacial meltwater pulls WW, a remnant of the preceding winter's sea-ice modified mixed layer, away from the freezing line and towards the mCDW-meltwater mixing line (the "Gade Line") (Figure 1c). These hydrographic properties suggest an underappreciated role for water mass transformation by sea-ice and glacial ice in the observed variability.

Informed by a high-resolution regional ocean simulation and the observations presented above, we introduce a simple overturning circulation model that represents the transformation of mCDW into cool thermocline waters both within the Dotson Ice Shelf cavity and at its entrance in the ASP. Using this model, we demonstrate that variations in polynya surface buoyancy fluxes, directly related to net local sea-ice formation rates, can generate large decadal scale thermocline depth variations in the absence of variable shelf-break forcing, posing an alternative mechanism for observed variability. The modeled thermocline variability takes the form of transitions between bistable warm and cool regimes, made possible by feedbacks between basal ice melt and stratification at the ice front. With this work, we underscore that variations in mCDW consumption, in addition to mCDW supply, can strongly influence the exposure of West Antarctic ice shelves to ocean heat. This work uses the Dotson Ice Shelf as a case study, however our model is applicable to other West Antarctic ice shelves fringed by coastal polynyas, including Venable and Pine Island ice shelves.
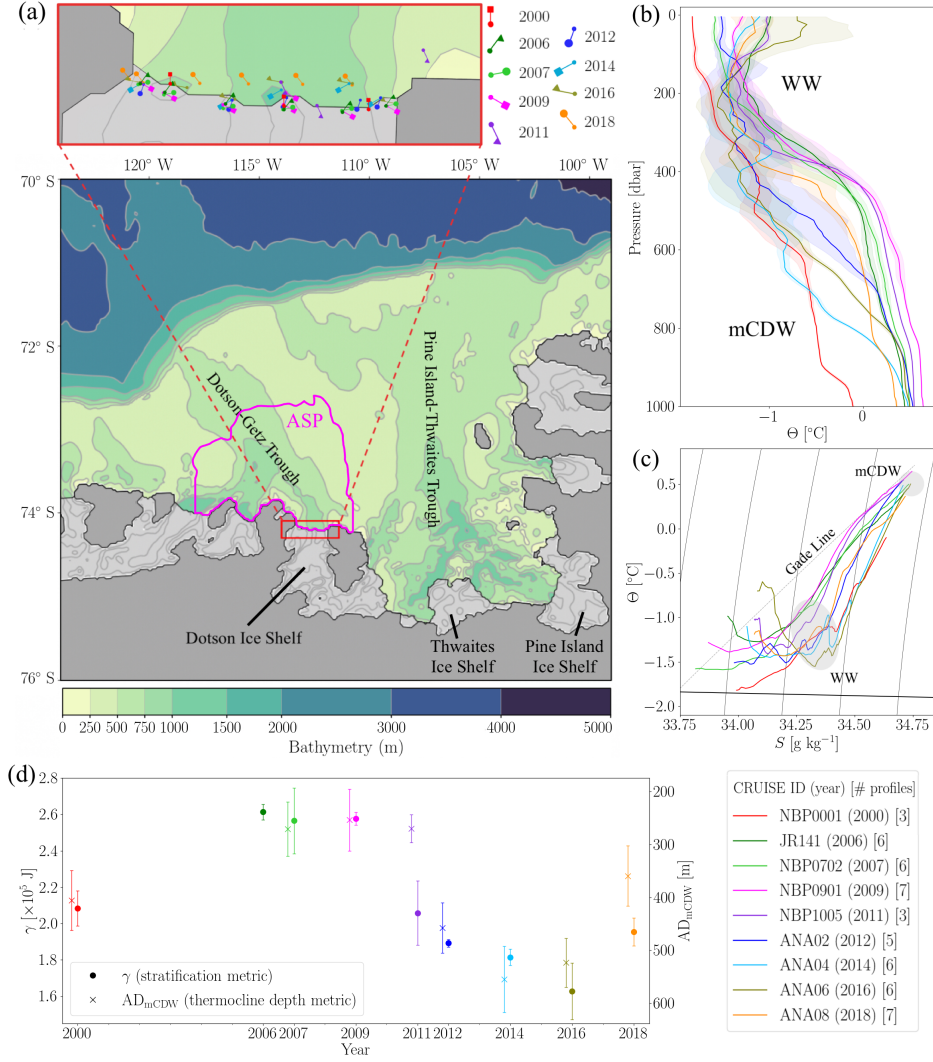
Figure 1. (a) Map of the Amundsen Sea embayment showing open ocean bathymetry (green shading; grey contours), ice shelf cavity bathymetry (grey shading; grey contours), and the grounded ice zone (dark grey). The Dotson Ice Front is outlined in red with an enlarged view provided above. The January climatological mean (2004-2022) extent of the Amundsen Sea Polynya (ASP) is indicated by the pink contour (using Fetterer & Stewart., 2020). Locations of shipborne observations used to produce (b)-(d) are indicated in the enlarged map. (b,c) Cruise mean conservative temperature (Θ) profiles as a function of pressure (b) and absolute salinity (S) (c). Mean profiles (solid lines) and standard deviations (shading) are calculated in density space and sorted into pressure space (as in Dutrieux et al., 2014) before being smoothed with a 5 dbar rolling mean. Water masses discussed in the main text (modified Circumpolar Deep Water, mCDW, and Winter Water, WW) are labelled. Potential density (black contours), the freezing line (thick black line), and an example Gade line indicative of mixing between mCDW and glacial meltwater (dashed black line) are shown for reference in (c). (d) Timeseries of γ, a bulk indicator of stratification strength calculated as the potential energy required to homogenize profiles between 5 and 750 dbars (circles), and the absolute depth of the mCDW layer AD_{mCDW}, a proxy for the thermocline depth developed by Kim et al. (2021) (crosses) (details in Supporting Information S1). AD_{mCDW} and γ values are offset on the time axis for clarity. Variables required for the calculation of AD_{mCDW} were not obtained for 2006. Observations were collected in the austral summer between December (previous year) and March (listed year).

2 Methods

2.1 Ice front overturning model

Motivated by observational evidence that the ice front thermocline depth is tied to basal melt rates (Jenkins et al., 2018) and that barotropic heat transport is blocked at the ice shelf front (Wåhlin et al., 2020), we present a purely baroclinic model for heat transport to ice shelves reminiscent of simple models for the global overturning (Walin, 1982; Gnanadesikan, 1999). This baroclinic model represents the shoreward transport of warm mCDW and export of cool surface water masses, including WW and glacially modified CDW, within Amundsen Sea glacially carved troughs (e.g. Webber et al., 2019). This exchange is facilitated by water mass transformation, which may occur within the ice shelf cavity or the ASP. Transformations are modeled in a small region proximate to the ice shelf front, isolating the effect of coastal forcing from shelf-break processes.

Key model components are illustrated in Figure 2. Warm mCDW and overlying thermocline waters are represented as boxes within the small region at the ice shelf front where winter polynya activity is concentrated (50 km meridional, 55 km zonal extent to match the width of the Dotson Ice Shelf). The inflow of warm mCDW, Ψ_{in}, is prescribed to represent remote wind-driven variations in shoreward mCDW transport. This mCDW then transforms into offshore flowing thermocline waters via two pathways: by melting glacial ice and mixing with the resultant meltwater in the ice shelf cavity (Ψ_{ice}) or by mixing with overlying waters (Ψ_{P}) (Figure 2a,b). Assuming negligible volume input from meltwater, the steady state transports balance,

$$\Psi_{\mathrm{in}} = \Psi_{\mathrm{ice}} + \Psi_{\mathrm{P}}. \tag{1}$$

The partitioning of mCDW transformation into Ψ_{ice} and Ψ_{P} is set by the thickness and relative buoyancy (i.e. stratification) of the mCDW and surface boxes. As illustrated in Figure 2c, the thermocline depth (h) and the thickness of the underlying mCDW layer (h_{mCDW}) evolve according to,

$$\frac{\mathrm{d}h}{\mathrm{d}t} = \frac{1}{L}\Big[\Psi_{\mathrm{ice}} + \Psi_{\mathrm{P}} - \Psi_{\mathrm{in}}\Big], \tag{2}$$

$$h_{\mathrm{mCDW}} = H - h, \tag{3}$$

where L is the meridional model extent and H is the ice front water column thickness (taken as 700 m). Ψ terms are converted from thickness fluxes to volume transports (1 Sv $= 10^6$ m^3 s^{-1}) via the model zonal extent. The buoyancy of the mCDW layer (b_{mCDW}) is kept constant, a choice justified by the minimal variability in mCDW density in observations (Figure 1c). We set

$$b_{\mathrm{mCDW}} = 0, \tag{4}$$

referencing our system to the buoyancy of the mCDW layer, such that the buoyancy differential between mCDW and thermocline waters, a metric for the ice front stratification strength, is $\Delta b = b - b_{\mathrm{mCDW}} = b$ where b is the buoyancy of thermocline waters. The stratification strength (Δb) then evolves according to the divergence of buoyancy fluxes from the thermocline (Figure 2c),

$$\frac{\mathrm{d}\Delta b}{\mathrm{d}t} = \frac{1}{L}\Big[(vb)_{\mathrm{in}} - (vb)_{\mathrm{out}}\Big] + \frac{1}{h}\Big[(wb)_{\mathrm{in}} - (wb)_{\mathrm{out}}\Big] \tag{5}$$

where,

$$(vb)_{\mathrm{in}} = \frac{\Psi_{\mathrm{ice}}\Delta b_{\mathrm{melt}}}{h}, \quad \text{and} \tag{6}$$

$$(vb)_{\mathrm{out}} = \frac{\Psi_{\mathrm{in}}\Delta b}{h}. \tag{7}$$

Δb_{melt} is the buoyancy of waters transformed by mixing with ice shelf meltwater, relative to b_{mCDW}, which we determine from hydrography to be 6.7×10^{-3} m s^{-2} (lightest waters in Figure 1c). The vertical buoyancy budget comprises a prescribed surface buoyancy flux due to net sea-ice formation in the polynya,

$$(wb)_{\mathrm{out}} = -F_{\mathrm{surf}} \tag{8}$$

(negative F_{surf} values lower surface ocean buoyancy) and buoyancy loss to the underlying mCDW layer due to mixing ($(wb)_{\mathrm{in}}$). We parameterize the latter as an advection-diffusion balance of buoyancy (e.g. Munk, 1966) which simplifies to

$$(wb)_{\mathrm{in}} = \frac{\Psi_{\mathrm{P}} b_{\mathrm{mCDW}}}{L} - \frac{\kappa_{\mathrm{P}}(b - b_{\mathrm{mCDW}})}{h} = -\frac{\kappa_{\mathrm{P}} \Delta b}{h}. \tag{9}$$

In (9) we select h as the most appropriate length-scale controlling vertical buoyancy transfer, since a thicker surface layer poses greater resistance to entrainment at its lower boundary when the primary energy source driving mixing is input at the surface.

The form of the polynya diffusivity term in (9), κ_{P}, is central to the feedbacks described in this study. Simply put, κ_{P} is a smoothed step function that transitions from a small diffusive end member κ_{diff} when the thermocline is buoyant to a large convective end member κ_{conv} when the thermocline approaches the density of the underlying mCDW. The effect is analogous to rapid transitions to vertical homogeneity triggered
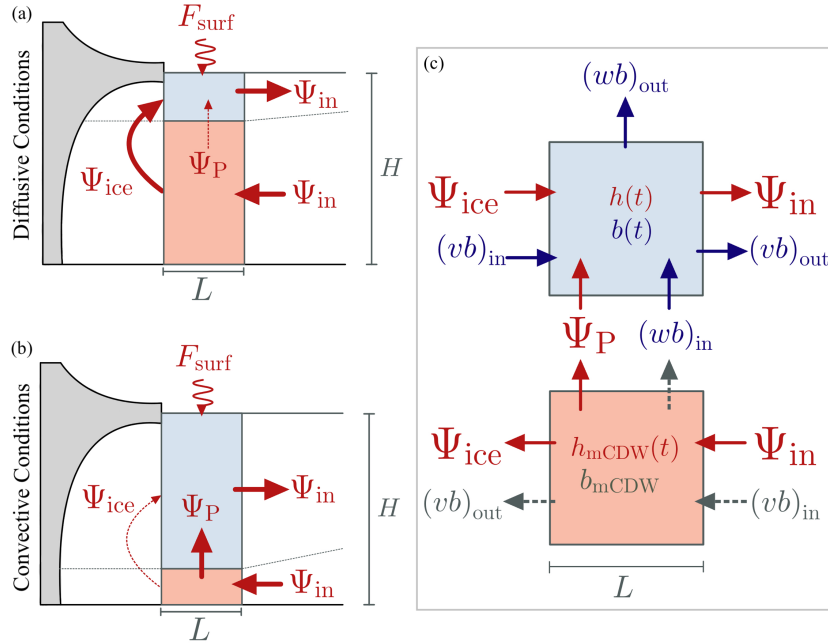
Figure 2. Schematic illustration of the ice front overturning model under (a) diffusive ($\kappa_{\mathrm{P}} \to \kappa_{\mathrm{diff}}$) and (b) convective ($\kappa_{\mathrm{P}} \to \kappa_{\mathrm{conv}}$) conditions. The thermocline and modified Circumpolar Deep Water (mCDW) layers are shaded blue and red respectively, and the ice shelf is shaded grey. Thick and dashed red arrows show the primary and secondary transformation pathways associated with each state. Thickness and buoyancy fluxes ($\Psi_{\mathrm{in}}, \Psi_{\mathrm{ice}}, \Psi_{\mathrm{P}}$ and F_{surf}) are indicated. (c) Schematic of the thickness and buoyancy budgets of the thermocline (upper; thickness and buoyancy evolved explicitly) and mCDW (lower; thickness evolved implicitly, buoyancy held constant) layers. The implied buoyancy budget of the mCDW layer is shown in grey, however b_{mCDW} does not evolve.

by static instability in simple models of open ocean polynyas (Martinson et al., 1981; Boot et al., 2021). Functionally, we define κ_P as,

$$\kappa_P(\Delta b) = \frac{\kappa_{conv} - \kappa_{diff}}{2}\Big(1 - \tanh\big(\phi(\Delta b - \Delta b_{crit})\big)\Big) + \kappa_{diff}, \qquad (10)$$

where κ_{conv} (10^{-2} m s^{-2}) and κ_{diff} (10^{-4} m s^{-2}, taken from summertime Pine Island Ice Front observations Garabato et al., 2017)(10^{-4} m s^{-2}) are vertical diffusivities, Δb_{crit} (5×10^{-4} m s^{-2}) is a small stratification strength at which turbulent convection onsets, and ϕ (5×10^{4}) is a parameter determining the steepness of the onset of convection. Our results are not sensitive to reasonable perturbations of the parameters.

The polynya mass transport term Ψ_P is constructed to be consistent with (9),

$$\Psi_P = -\frac{\kappa_P L}{h}. \qquad (11)$$

Finally, the ice cavity overturning Ψ_{ice} is taken to be linearly proportional to the mCDW thickness,

$$\Psi_{ice} = \alpha h_{mCDW} = \alpha(H - h), \qquad (12)$$

where α (2.1×10^{-3} m s^{-1}) is diagnosed from the WAIS 1080 regional simulation (see §2.2 and Supporting Information S2).

To summarize, the ice front overturning model is described by the following coupled differential equations for the thermocline depth (h) and stratification strength (Δb),

$$\frac{dh}{dt} = \frac{1}{L}\Big[\alpha(H - h) - \frac{\kappa_P L}{h} - \Psi_{in}\Big], \qquad (13)$$

$$\frac{d\Delta b}{dt} = \frac{1}{Lh}\Big[\alpha(H - h)\Delta b_{melt} - \Psi_{in}\Delta b\Big] + \frac{1}{h^2}\Big[F_{surf}h - \kappa_P \Delta b\Big]. \qquad (14)$$

All parameter values except the diffusivity κ_P are diagnosed from observations or WAIS 1080 (§2.2), and Ψ_{in} and F_{surf} are prescribed forcings representing the supply of mCDW (a remote forcing) and polynya surface buoyancy fluxes from sea ice(a local forcing).

2.2 Regional general circulation model

In addition to the ice front overturning model, we utilize monthly mean output from WAIS 1080, a high-resolution (~ 3 km horizontal spacing) regional numerical ocean model, based on the Massachusetts Institute of Technology general circulation model (MITgcm), that represents the tip of the Antarctic Peninsula to the western edge of the Amundsen Sea (Flexas et al., 2022). The model is forced at the surface by the European Centre for Medium-Range Weather Forecasts (ECMWF) reanalysis version 5 (ERA5; Hersbach et al., 2020) and integrated from 1992 to 2019. WAIS 1080 explicitly represents freezing and melting within ice shelf cavities of a fixed shape, making it suited to the study of ocean ice-shelf interactions at relatively short timescales. We use the control simulation from Flexas et al. (2022), who provide additional model details, to constrain the values of parameters (α) and forcings (F_{surf}, Ψ_{in}) of the ice front overturning model that are difficult to obtain directly from observations. Details of how α, F_{surf}, and Ψ_{in} values are obtained from WAIS 1080 are provided in Supporting Information S2.

3 Results

3.1 Steady state model behavior

Equilibrated solutions of the ice front overturning model map a hysteresis loop for the thermocline depth in response to varying surface buoyancy forcing (F_{surf}) when the supply of mCDW from the shelf-break (Ψ_{in}) is held fixed (Figure 3a). Thus, warm and

cold regimes can be realized with the same mCDW supply. This hysteresis loop is enabled by a positive feedback between the depth of the ice front thermocline and the stratification of the ice front water column, the physics of which are parameterized in our vertical diffusivity term κ_{P}. A shallow ice front thermocline, equivalent to a thick mCDW layer, supports high melt rates within the cavity. The ensuing meltwater provides an additional buoyancy input to the thermocline that suppresses convection and reinforces the shallow thermocline position (upper "branch" of the hysteresis loop, Figure 3a). By contrast, a deep ice front thermocline, equivalent to a thin mCDW layer, is associated with a weaker ice shelf melt rate and a reduced input of buoyant meltwater to the WW layer, comparatively preconditioning the water column for convection and reinforcing the deep thermocline position (lower "branch", Figure 3a). This feedback produces bistable "diffusive" ($\kappa_{\mathrm{P}} = \kappa_{\mathrm{diff}}$, thick mCDW) and "convective" ($\kappa_{\mathrm{P}} = \kappa_{\mathrm{conv}}$, thin mCDW) steady states for a fixed supply of mCDW associated with an $\sim$ (400 m) thermocline depth differential. In this idealized model, most convective steady states are unstably stratified ($b_{\mathrm{WW}} < 0$, i.e. $b_{\mathrm{WW}} < b_{\mathrm{mCDW}}$) as they arise when strong negative buoyancy forcing is continuously applied. These bistable states have comparable mCDW depths to the ob-
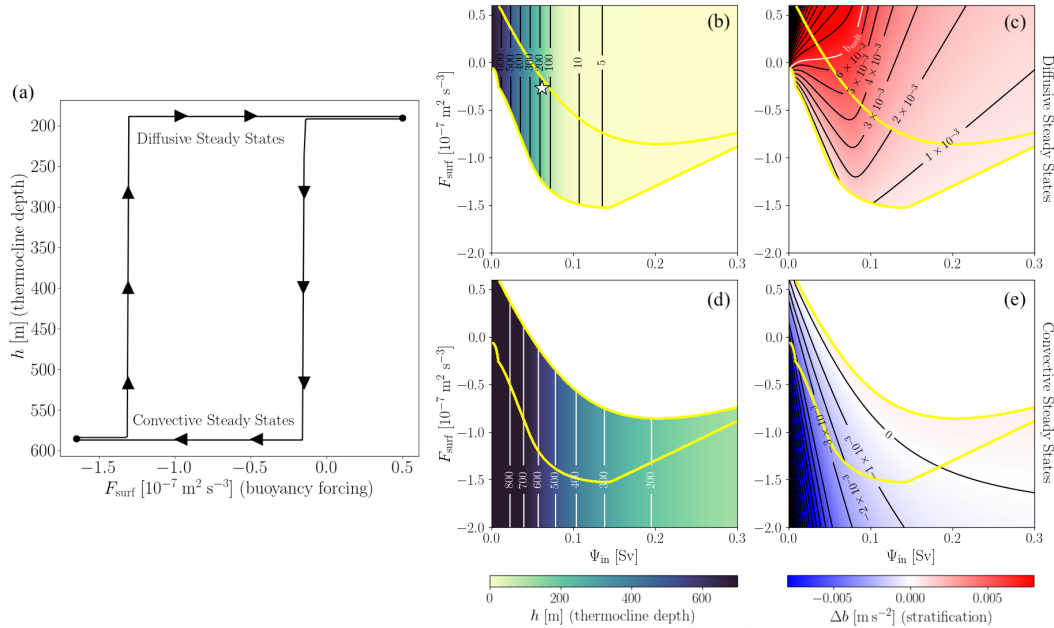
Figure 3.   (a) Dependence of the model steady state on F_{surf} when Ψ_{in} is held fixed at the mean WAIS 1080 value (0.06 Sv). The model is evolved to steady state after incrementally increasing and decreasing values of F_{surf} (direction indicated by arrows) spanning the range simulated in WAIS 1080. The forward and reverse pathways are offset to aid visualization. Text inset identifies solutions associated with $\kappa_{\mathrm{P}} = \kappa_{\mathrm{conv}}$ ("convective steady states") and $\kappa_{\mathrm{P}} = \kappa_{\mathrm{diff}}$ ("diffusive steady states"). (b-e) Plots showing equilibrated h (b,d) and Δb (c,e) values associated with diffusive steady states (b,c) and convective steady states (d,e) for a range of Ψ_{in} and F_{surf} forcing values. Regions of each phase space left white do not support steady states with the relevant κ_{P} value. Yellow contours outline the parameter space able to support both diffusive and convective steady states. The white star in (b) shows the time mean WAIS 1080 forcing. Convective steady states to with $h > 700$ m (depth of the water column) are not physical, but are shown here since transient forcing in this region is permissible.

served warm and cool phases (Figure 1d), although observed cool phases, which are sampled exclusively during summer months, are stably stratified.

Bistability occurs over a large portion of the explored forcing space (yellow contour in Figure 3b-e), which spans realistic ranges of F_{surf} and Ψ_{in} (monthly mean values span $-1.7{\times}10^{-7}$ to $0.5{\times}10^{-7}$ m^2 s^{-3} and 0 to 0.3 Sv in WAIS 1080). Forcing combinations that support only one steady state solution are referred to as monostable. Figure 3b-e suggests variations in both F_{surf} (vertical paths in Figure 3b-e) and Ψ_{in} (horizontal paths) can generate hysteresis by shifting the system from one monostable region to the other via the bistable region. Whilst Figure 3 displays numerically equilibrated model output, a benefit of this model's simplicity is that it permits analytical solutions for end member cases and easy exploration of parameter space (Supporting Information S3). Overall, model behavior is not qualitatively sensitive to reasonable parameter perturbations; a summary of our sensitivity assessment appears in Table S1.

3.2 Transient model behavior

The presence of bistability in this simple model poses an alternate explanation for the decadal scale ~ 400 m thermocline depth variations observed at the Dotson Ice Front. The observed variability could, as previously implied, be a low frequency response to low frequency variations in the supply of mCDW to the ice front. Alternatively, our simple model suggests that transient perturbations of either mCDW supply or coastal surface buoyancy fluxes could trigger transitions between self-reinforcing deep and shallow thermocline states, perhaps explaining the large amplitude and persistent nature of the observed cool and warm phases. This possibility is tested with transiently forced experiments.

The ice front overturning model is initialized with either weak or strong stratification and forced with WAIS 1080 climatological mean F_{surf} and Ψ_{in} values until annual patterns of ice front stratification (Δb) and thermocline depth (h) equilibrate. The WAIS 1080 climatology lies sufficiently within the bistable forcing region (yellow shaded region in Figure 4a,b) to support temporally varying solutions that persist in their initial diffusivity regime. These equilibrated simulations are then transiently forced with perturbed climatologies to prompt regime transitions that persist when the forcing returns to the original pattern. Two winter perturbations are constructed by decreasing the May-September F_{surf} or Ψ_{in} forcing by a constant offset, and two summer perturbations are constructed by increasing the December-April F_{surf} or Ψ_{in} forcing by a constant offset. Winter and summer perturbations are then tested for their ability to drive transitions from the diffusive to the convective regime and vice versa. Seasonal perturbations are chosen based on the strong seasonality of F_{surf}; we also use a seasonal perturbation for Ψ_{in} experiments for consistency, although Ψ_{in} has a more complex annual pattern (Figure 4b inset).

Figure 4a,b show the smallest amplitude winter and summer offsets that trigger regime shifts within two consecutive years of perturbed forcing. When regime transitions are simulated (Figure 4c,e,f), lags between the thermocline response and stratification response align with observations. In agreement with the observed transition from a warm phase to a cool phase between 2009 and 2012 (Figure 1d), thermocline depth anomalies lag buoyancy anomalies during modeled transitions to convective conditions (Figure 4c). The shoaled thermocline observed in 2018 may represent a transition to warm phase conditions with the opposite lag, thermocline shoaling preceding stratification strengthening. If so, the simulated lags between thermocline depth anomalies and buoyancy anomalies in both Ψ_{in} and F_{surf}-driven transitions to diffusive conditions (Figure 4d,e) are also consistent with observations.

In addition to capturing the nature of observed transitions between warm and cool phases at the Dotson Ice Front, our idealized model anticipates the shallow bias and di-

minished variability of the ice front thermocline depth in WAIS 1080 (0°C isotherm depth ranges from 440-820 m in observations and only 255-420 m in WAIS 1080). When the ice front overturning model is forced with the full WAIS 1080 1992-2019 timeseries of F_{surf} and Ψ_{in}, rather than climatological values, simulations initialized with convective conditions rapidly transition to diffusive conditions and remain there (Figure S5), consistent with WAIS 1080 failing to capture convective events. In general, transitions to convective states required larger deviations from the WAIS 1080 forcing than transitions to diffusive states. Significantly stronger negative F_{surf} values than those simulated in WAIS 1080 were needed to generate a regime shift within a single year (minimum winter values of -3×10^{-7} m^2 s^{-3} compared to minimum WAIS 1080 forcing of -1.7×10^{-7} m^2 s^{-3}), thus our choice to present results of two-year perturbations in Figure 4. ERA5 has been shown to underestimate near-surface wind speeds along the Antarctic coastline (Caton Harrison et al., 2022) and this may induce an underestimation of winter F_{surf} minima in WAIS 1080, alternatively, WAIS 1080 and our idealized model may exaggerate the barrier to convection.

Reductions in Ψ_{in}, whether transient (Figure 4d) or more sustained (Figure S6), do not trigger transitions to convective conditions for any physical choice of offset (i.e. enforcing $\Psi_{\mathrm{in}} > 0$). Such regime shifts are not supported as reducing Ψ_{in} initially strengthens ice front stratification in our simulations. This anticorrelation between thermocline depth and stratification when Ψ_{in} is reduced is not supported by observations or WAIS 1080, however, and may reflect the simplicity of our model. These experiments affirm the possibility that polynya forcing can drive realistic transitions to cool phases, but do not negate the possibility that variable mCDW supply could also drive such transitions. Both forcings appear able to drive realistic transitions to warm conditions.

4 Discussion and Outlook

This study intentionally targets a simplified representation of West Antarctic coastal ocean dynamics to highlight mechanistic links between surface forcing, interior mixing, thermocline depth variations, and overturning pathways on the West Antarctic continental shelf. The key result is the identification of positive feedbacks that are independent of the supply of mCDW from the continental shelf break. These dynamics involve interactions between basal ice shelf melt rates and thermocline stratification at the ice shelf front, and provide a plausible explanation for the amplitude and duration of multi-year warm and cool phases observed, for example, at the Dotson Ice Front. The modeled thermocline variability tracks the strength of convection in the adjacent coastal polynya and successfully reproduces observed stratification changes, not previously identified, associated with transitions between the warm and cool phases. These low frequency variations in convection may arise either from a variable mCDW supply from the continental shelf break (a remote forcing), or from surface buoyancy fluxes within the polynya (a local forcing). Since future trends in mCDW supply from the shelf-break and sea-ice production in coastal polynyas may not align, understanding the relative importance of these forcings is important for projecting future melt. Critically, the positive feedback identified here cannot be represented in complex ocean models that apply fixed meltwater inputs. This study motivates analysis in models that simulate basal melt within cavities. As a first step on this path, we show that the the idealized model predicts the shallow, steady bias of the Dotson Ice Front thermocline in the WAIS 1080 model based on its forcing, demonstrating the power of using a combination of idealized and complex models to characterize model biases. Additionally, our results point to ice front stratification as a key target diagnostic for simulations of West Antarctic ocean-forced ice shelf melt. Finally, this study emphasizes the importance of water mass transformation, both over the shelf and in ice shelf cavities, as a key process that links shelf-break and coastal processes through closure of the shelf overturning circulation.
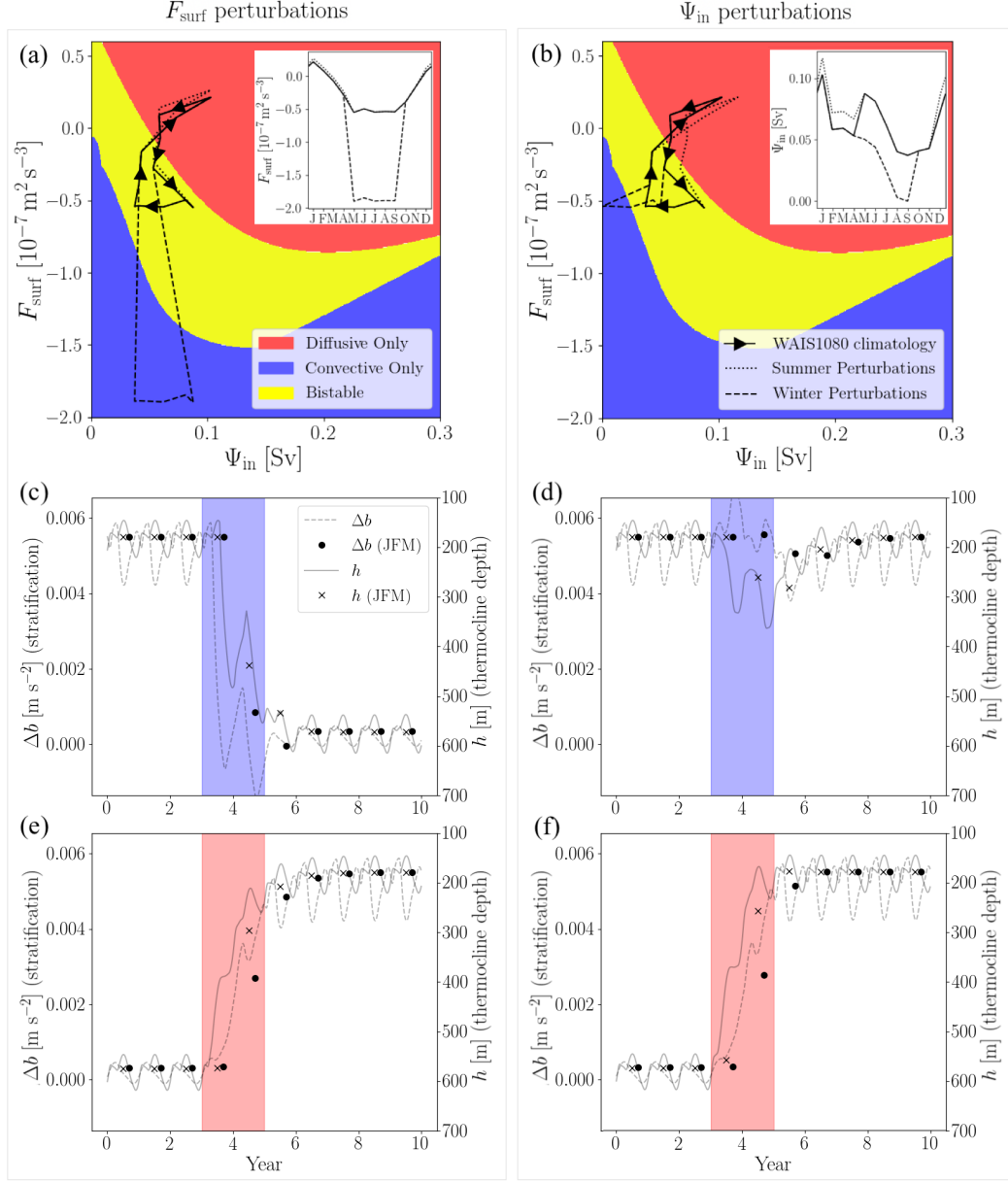
Figure 4. (a, b) The forcing parameter space partitioned into regions supporting only one steady state solution (diffusive in red; convective in blue) and both solutions (bistability in yellow). Climatological mean F_{surf} and Ψ_{in} values from the WAIS 1080 simulation are shown within this forcing space (solid black lines) with arrows indicating the progression of an annual cycle. Winter perturbed forcings (dashed lines) and summer perturbed forcings (dotted lines) are indicated within the forcing space for F_{surf} experiments (a) and Ψ_{in} experiments (b). Forcing climatologies are shown as a function of time in inset panels for clarity. (c-f) Full time series of h (solid grey lines) and Δb (dashed grey lines) alongside January-March mean values (black crosses and circles, respectively) from transient forcing experiments described in the main text. Shaded regions indicate the perturbation period (years 4 and 5) and whether a winter (blue; c,d) or summer (red; e,f) perturbation was prescribed.

The idealized representation of coastal dynamics in this study neglects certain processes that merit discussion. The most notable simplification is that WW, meltwater modified CDW, and other surface waters are combined in a single box. As a result, the spatial structure of glacial meltwater plumes exiting the cavity (e.g. Garabato et al., 2017; Zheng et al., 2021) and exiting the model domain are omitted, and buoyancy from meltwater is uniformly distributed above the thermocline. This simplification may lead to spurious stratification strengthening in response to reductions in mCDW supply (Figure 4d), as unresolved structures may remove meltwaters from the ice shelf front more rapidly than our model suggests. The truncated vertical structure of our model also leads to unrealistic year-round convection during cool phases in transiently forced simulations (Figure 4). In the real ocean, positive F_{surf} forcing during summer months may halt convection by stratifying a small fraction of the upper water column whilst leaving the deep thermocline position intact. In our model, positive buoyancy fluxes are distributed over the full thermocline depth, presenting an exaggerated barrier to restratification. Consequently, the water column convects year-round rather than being preconditioned for the annual recurrence of convection. Another noteworthy simplification is that, since Ψ_{in} and F_{surf} are prescribed, we neglect feedbacks that influence their magnitude. Shoreward mCDW transport in the Amundsen Sea may decrease (Moorman et al., 2020; Beadling et al., 2022) or increase (Si et al., 2023) in response to coastal freshening, and coastal sea-ice formation rates may likewise be sensitive to coastal freshening by meltwater. Further work is necessary to synthesize these complex responses to changing melt rates and simple models, such as the one presented here, may be useful tools in this effort. The ability for our idealized model to capture key features of observed Amundsen Sea mCDW variability despite these simplifications speaks to the importance of ice front thermocline stratification strength to ocean-driven glacial melt variability on decadal timescales.

This work builds on regional modeling (St-Laurent et al., 2015; Caillet et al., 2022; Naughten et al., 2022), idealized modeling (Petty et al., 2013; Silvano et al., 2018), and observational evidence (Webber et al., 2017) indicating coastal buoyancy forcing can modulate ocean heat availability at West Antarctic ice shelves. In agreement with our findings, anomalously strong coastal surface buoyancy fluxes can explain the 2011-2013 cool period observed at the Pine Island Ice Front (St-Laurent et al., 2015; Webber et al., 2017). At longer timescales, simulated deep coastal warming trends have been associated with centennial scale reductions in coastal convection (Naughten et al., 2022), and simulated transitions between more dramatic cool and warm Amundsen shelf states closely track surface buoyancy forcing changes (Caillet et al., 2022). Idealized models, on the other hand, have primarily been used to assess the Amundsen Sea mean state, with bulk mixed layer models indicating a leading role for buoyancy fluxes in setting the shallow winter mixed layer depths typical of the West Antarctic shelf relative to other Antarctic regions (Petty et al., 2013; Silvano et al., 2018). Whilst Amundsen Sea variability at interannual and longer timescales has not been targeted with idealized models, there is precedent elsewhere. For example, conceptual models have been used to interrogate bistable low and high melt states of the Filchner-Ronne Ice Shelf enabled by coastal buoyancy feedbacks analogous to those identified here (Hazel & Stewart, 2020). Our approach incorporates the consideration of buoyancy central to these results into a "thermocline model" framework based on closing watermass transformation pathways, a framework originally applied to the global overturning circulation (e.g. Gnanadesikan, 1999; Marshall & Zanna, 2014; Thompson et al., 2019).

We take away two important lessons for future studies of warm West Antarctic shelf seas. Firstly, the dynamics that govern the exposure of ice shelves to ocean heat must account not only for variability in mCDW supply, but also mCDW consumption or transformation, with the latter having received significantly less attention. Secondly, we cannot neglect the dynamical effects of meltwater in a salinity stratified system; ongoing observational monitoring and accurate simulation of ice front stratification strength should be prioritized.

Open Research Section

Data and code required to reproduce all figures in the main text and Supporting Information provided at `https://doi.org/10.5281/zenodo.7987113`. A binder environment (see `https://mybinder.org/` for details) has been constructed so that readers can open, edit, and execute all code from a browser (click "launch binder" button on the GitHub repository home page linked to the listed doi). Editing within the binder environment will not alter the original file, so readers should feel free to manipulate provided code.

Acknowledgments

References

Adusumilli, S., Fricker, H. A., Medley, B., Padman, L., & Siegfried, M. R. (2020). Interannual variations in meltwater input to the southern ocean from antarctic ice shelves. *Nature geoscience*, *13*(9), 616–620.

Assmann, K. M., Jenkins, A., Shoosmith, D. R., Walker, D. P., Jacobs, S. S., & Nicholls, K. W. (2013). Variability of circumpolar deep water transport onto the Amundsen Sea Continental shelf through a shelf break trough. *Journal of Geophysical Research: Oceans*, *118*(12), 6603–6620. doi: 10.1002/2013JC008871

Beadling, R., Krasting, J., Griffies, S., Hurlin, W., Bronselaer, B., Russell, J., . . . Winton, M. (2022). Importance of the antarctic slope current in the southern ocean response to ice sheet melt and wind stress change. *Journal of Geophysical Research: Oceans*, *127*(5), e2021JC017608.

Boot, D., Van Westen, R. M., & Dijkstra, H. A. (2021, feb). Multidecadal polynya formation in a conceptual (box) model. *Ocean Science*, *17*(1), 335–350. doi: 10.5194/os-17-335-2021

Caillet, J., Jourdain, N. C., Mathiot, P., Hellmer, H. H., & Mouginot, J. (2022). Drivers and reversibility of abrupt ocean state transitions in the amundsen sea, antarctica. *Journal of Geophysical Research: Oceans*, e2022JC018929.

Caton Harrison, T., Biri, S., Bracegirdle, T. J., King, J. C., Kent, E. C., Vignon, É., & Turner, J. (2022). Reanalysis representation of low-level winds in the antarctic near-coastal region. *Weather and Climate Dynamics*, *3*(4), 1415–1437.

Dotto, T. S., Garabato, A. C., Bacon, S., Holland, P. R., Kimura, S., Firing, Y. L., . . . Jenkins, A. (2019). Wind-driven processes controlling oceanic heat delivery to the amundsen sea, antarctica. *Journal of Physical Oceanography*, *49*(11), 2829–2849. doi: 10.1175/JPO-D-19-0064.1

Dotto, T. S., Garabato, A. C. N., Wåhlin, A. K., Bacon, S., Holland, P. R., Kimura, S., . . . Jenkins, A. (2020). Control of the Oceanic Heat Content of the Getz-Dotson Trough, Antarctica, by the Amundsen Sea Low. *Journal of Geophysical Research: Oceans*, *125*(8), e2020JC016113. doi: 10.1029/2020JC016113

Dutrieux, P., De Rydt, J., Jenkins, A., Holland, P. R., Ha, H. K., Lee, S. H., . . . Schröder, M. (2014). Strong sensitivity of Pine Island ice-shelf melting to cli-

matic variability. *Science*, *343*(6167), 174–178. doi: 10.1126/science.1244341

Fetterer, F., & Stewart., J. S. (2020). *U.S. National Ice Center Arctic and Antarctic Sea Ice Concentration and Climatologies in Gridded Format, Version 1.* National Snow and Ice Data Center. Retrieved from https://nsidc.org/data/g10033/versions/1 doi: 10.7265/46cc-3952

Flexas, M. M., Thompson, A. F., Schodlok, M. P., Zhang, H., & Speer, K. (2022). Antarctic peninsula warming triggers enhanced basal melt rates throughout west antarctica. *Science Advances*, *8*(31), eabj9134.

Fretwell, P., Pritchard, H. D., Vaughan, D. G., Bamber, J. L., Barrand, N. E., Bell, R., ... others (2013). Bedmap2: improved ice bed, surface and thickness datasets for antarctica. *The cryosphere*, *7*(1), 375–393.

Fürst, J. J., Durand, G., Gillet-Chaulet, F., Tavard, L., Rankl, M., Braun, M., & Gagliardini, O. (2016). The safety band of Antarctic ice shelves. *Nature Climate Change*, *6*(5), 479–482. doi: 10.1038/NCLIMATE2912

Garabato, A. C. N., Forryan, A., Dutrieux, P., Brannigan, L., Biddle, L. C., Heywood, K. J., ... Kimura, S. (2017). Vigorous lateral export of the meltwater outflow from beneath an antarctic ice shelf. *Nature*, *542*(7640), 219–222.

Gnanadesikan, A. (1999). A simple predictive model for the structure of the oceanic pycnocline. *Science*, *283*(5410), 2077–2079. doi: 10.1126/science.283.5410.2077

Hazel, J. E., & Stewart, A. L. (2020, apr). Bistability of the Filchner-Ronne Ice Shelf Cavity Circulation and Basal Melt. *Journal of Geophysical Research: Oceans*, *125*(4), e2019JC015848. doi: 10.1029/2019JC015848

Hersbach, H., Bell, B., Berrisford, P., Hirahara, S., Horányi, A., Muñoz-Sabater, J., ... others (2020). The era5 global reanalysis. *Quarterly Journal of the Royal Meteorological Society*, *146*(730), 1999–2049.

IMBIE Team. (2018). Mass balance of the Antarctic Ice Sheet from 1992 to 2017. *Nature 2018 558:7709*, *558*(7709), 219–222. doi: 10.1038/s41586-018-0179-y

Jenkins, A., Dutrieux, P., Jacobs, S., Steig, E. J., Gudmundsson, G. H., Smith, J., & Heywood, K. J. (2016). Decadal Ocean Forcing and Antarctic Ice Sheet Response: LESSONS FROM THE AMUNDSEN SEA. *Oceanography*, *29*(4), 106–117.

Jenkins, A., Shoosmith, D., Dutrieux, P., Jacobs, S., Kim, T. W., Lee, S. H., ... Stammerjohn, S. (2018). West Antarctic Ice Sheet retreat in the Amundsen Sea driven by decadal oceanic variability. *Nature Geoscience*, *11*(10), 733–738. doi: 10.1038/s41561-018-0207-4

Kim, T. W., Ha, H. K., Wåhlin, A. K., Lee, S. H., Kim, C. S., Lee, J. H., & Cho, Y. K. (2017, jan). Is Ekman pumping responsible for the seasonal variation of warm circumpolar deep water in the Amundsen Sea? *Continental Shelf Research*, *132*, 38–48. doi: 10.1016/j.csr.2016.09.005

Kim, T.-W., Yang, H. W., Dutrieux, P., Wåhlin, A. K., Jenkins, A., Kim, Y. G., ... Cho, Y.-K. (2021). Interannual Variation of Modified Circumpolar Deep Water in the Dotson-Getz Trough, West Antarctica. *Journal of Geophysical Research: Oceans*, *126*(12), e2021JC017491.

Marshall, D. P., & Zanna, L. (2014). A conceptual model of ocean heat uptake under climate change. *Journal of Climate*, *27*(22), 8444–8465.

Martinson, D. G., Killworth, P. D., & Gordon, A. L. (1981). A convective model for the weddell polynya. *Journal of Physical Oceanography*, *11*(4), 466–488.

Moorman, R., Morrison, A. K., & McC. Hogg, A. (2020). Thermal responses to antarctic ice shelf melt in an eddy-rich global ocean–sea ice model. *Journal of Climate*, *33*(15), 6599–6620.

Morlighem, M., Rignot, E., Binder, T., Blankenship, D., Drews, R., Eagles, G., ... Young, D. A. (2020). Deep glacial troughs and stabilizing ridges unveiled beneath the margins of the Antarctic ice sheet. *Nature Geoscience*, *13*(2), 132–137. doi: 10.1038/s41561-019-0510-8

Mouginot, J., Rignot, E., & Scheuchl, B. (2014). Sustained increase in ice discharge from the amundsen sea embayment, west antarctica, from 1973 to 2013. *Geophysical Research Letters*, *41*(5), 1576–1584.

Munk, W. H. (1966). Abyssal recipes. In *Deep sea research and oceanographic abstracts* (Vol. 13, pp. 707–730).

Naughten, K. A., Holland, P. R., Dutrieux, P., Kimura, S., Bett, D. T., & Jenkins, A. (2022). Simulated twentieth-century ocean warming in the amundsen sea, west antarctica. *Geophysical Research Letters*, *49*(5), e2021GL094566.

Paolo, F. S., Fricker, H. A., & Padman, L. (2015). Volume loss from antarctic ice shelves is accelerating. *Science*, *348*(6232), 327–331. doi: 10.1126/science .aaa0940

Petty, A. A., Feltham, D. L., & Holland, P. R. (2013). Impact of atmospheric forcing on antarctic continental shelf water masses. *Journal of Physical Oceanography*, *43*(5), 920–940.

Pritchard, H., Ligtenberg, S. R., Fricker, H. A., Vaughan, D. G., van den Broeke, M. R., & Padman, L. (2012). Antarctic ice-sheet loss driven by basal melting of ice shelves. *Nature*, *484*(7395), 502–505.

Schmidtko, S., Heywood, K. J., Thompson, A. F., & Aoki, S. (2014). Multidecadal warming of antarctic waters. *Science*, *346*(6214), 1227–1231.

Shepherd, A., Wingham, D., & Rignot, E. (2004). Warm ocean is eroding west antarctic ice sheet. *Geophysical Research Letters*, *31*(23).

Si, Y., Stewart, A. L., & Eisenman, I. (2023). Heat transport across the antarctic slope front controlled by cross-slope salinity gradients. *Science Advances*, *9*(18), eadd7049.

Silvano, A., Holland, P. R., Naughten, K. A., Dragomir, O., Dutrieux, P., Jenkins, A., . . . others (2022). Baroclinic ocean response to climate forcing regulates decadal variability of ice-shelf melting in the amundsen sea. *Geophysical Research Letters*, *49*(24), e2022GL100646.

Silvano, A., Rintoul, S. R., Peña-Molino, B., Hobbs, W. R., Van Wijk, E., Aoki, S., . . . Williams, G. D. (2018, apr). Freshening by glacial meltwater enhances melting of ice shelves and reduces formation of Antarctic Bottom Water. *Science Advances*, *4*(4), eaap9467. doi: 10.1126/sciadv.aap9467

St-Laurent, P., Klinck, J. M., & Dinniman, M. S. (2015). Impact of local winter cooling on the melt of Pine Island Glacier, Antarctica. *Journal of Geophysical Research: Oceans*, *120*(10), 6718–6732. doi: 10.1002/2015JC010709

Thompson, A. F., Hines, S. K., & Adkins, J. F. (2019). A southern ocean mechanism for the interhemispheric coupling and phasing of the bipolar seesaw. *Journal of Climate*, *32*(14), 4347–4365.

Turner, J., Orr, A., Gudmundsson, G. H., Jenkins, A., Bingham, R. G., Hillenbrand, C.-D., & Bracegirdle, T. J. (2017). Atmosphere-ocean-ice interactions in the amundsen sea embayment, west antarctica. *Reviews of Geophysics*, *55*(1), 235–276.

Wåhlin, A. K., Steiger, N., Darelius, E., Assmann, K. M., Glessmer, M. S., Ha, H. K., . . . Viboud, S. (2020). Ice front blocking of ocean heat transport to an Antarctic ice shelf. *Nature*, *578*(7796), 568–571. doi: 10.1038/ s41586-020-2014-5

Walin, G. (1982). On the relation between sea-surface heat flow and thermal circulation in the ocean. *Tellus*, *34*(2), 187–195.

Walker, D. P., Brandon, M. A., Jenkins, A., Allen, J. T., Dowdeswell, J. A., & Evans, J. (2007). Oceanic heat transport onto the Amundsen Sea shelf through a submarine glacial trough. *Geophysical Research Letters*, *34*(2). doi: 10.1029/2006GL028154

Webber, B. G., Heywood, K. J., Stevens, D. P., & Assmann, K. M. (2019). The impact of overturning and horizontal circulation in pine Island trough on ice shelf melt in the eastern Amundsen Sea. *Journal of Physical Oceanography*,

49(1), 63–83. doi: 10.1175/JPO-D-17-0213.1

Webber, B. G., Heywood, K. J., Stevens, D. P., Dutrieux, P., Abrahamsen, E. P., Jenkins, A., . . . Kim, T. W. (2017). Mechanisms driving variability in the ocean forcing of Pine Island Glacier. *Nature Communications*, *8*(1), 1–8. doi: 10.1038/ncomms14507

Zheng, Y., Heywood, K. J., Webber, B. G., Stevens, D. P., Biddle, L. C., Boehme, L., & Loose, B. (2021). Winter seal-based observations reveal glacial meltwater surfacing in the southeastern amundsen sea. *Communications Earth & Environment*, *2*(1), 40.

Supporting Information for "Coastal polynyas enable transitions between high and low West Antarctic ice shelf melt rates"

Ruth Moorman[1], Andrew F. Thompson[1], and Earle A. Wilson[2]

[1]Environmental Science and Engineering, California Institute of Technology, Pasadena, California, USA

[2]Department of Earth System Science, Stanford University, Stanford, California, USA

Contents of this file

1. Text S1 to S3

2. Figures S1 to S6

3. Table S1

Introduction The SI includes a summary of techniques used to analyze the historical observational data sets employed in this study (S1), the methods for deriving model parameters and forcing fields from the WAIS 1080 numerical output (S2, Figures S1-3), a brief summary of how the idealized model responds to parameter perturbations (S3, Figure S4), and two additional transiently forced simulations not included in the main text (Figures S5-6). We refer to Jupyter Notebooks, provided in linked GitHub repository (`https://github.com/ruth-moorman/Moorman-et-al-GRL-submission-2023`) accompanied by a binder environment so that readers can open, edit, and execute all code from a browser.

————

May 26, 2023, 10:48pm

Text S1.

Here we provide details of the γ and $\mathrm{AD_{mCDW}}$ metrics presented in Figure 1d.

Following Simpson, Allen, and Morris (1978) and Venables and Meredith (2014), we define the stratification metric γ as the potential energy of the water column relative to the potential energy of a mixed water column. This choice is made in lieu of buoyancy frequency metrics, which are found to be sensitive to an arbitrary choice of thermocline depth. The diagnosed potential energy is effectively the energy input required to homogenize the water column to a given depth. Functionally, this metric γ is defined as

$$\gamma = \int_{h_2}^{h_1} (\rho - \langle \rho \rangle) gz \, dz \quad \text{where} \quad \langle \rho \rangle = \frac{1}{h_2 - h_1} \int_{h_2}^{h_1} \rho \, dz. \tag{1}$$

We take h_1 to be a near surface depth (5 m) and h_2 to be a depth sufficiently deep to be typically located below the thermocline yet shallow enough so that the deepest measurement in at least half of the 49 profiles used in this study exceed h_2 (here 750 m). For a vertically mixed column, $\gamma = 0$ with γ growing increasingly positive for increasingly stable stratification. Only those profiles with a maximum depth exceeding h_2 are used in the calculation of γ, since the value of the integrated metric is artificially reduced by missing values. At least 2 profiles meet this criterion for each cruise year and the choice $h_2 = 750$ m. The temporal pattern is not sensitive to reasonable perturbations (up to and greater than 100 m) of h_1 and h_2. Interactive code used to compute this metric and test its sensitivity to h_1 and h_2 are available in the notebook "Figure1.ipynb" of the provider jupyter binder environment and GitHub repository.

Details of the metric used for the depth of the mCDW layer, $\mathrm{AD_{mCDW}}$, are provided in Kim et al. (2021) and the "Figure1.ipynb" notebook. The method simultaneously solves

for volume fractions of mCDW, WW, and glacial meltwater, comprising each point of a vertical profile of temperature, salinity, and dissolved oxygen given end member characteristics of the three water masses. Volume fractions are then vertically integrated and AD_{mCDW} is taken as the depth of the profile minus the integrated mCDW volume fraction. Thermocline depths calculated by this method are shallow biased relative to a visual identification of thermoclines identified from temperature profiles, as WW is modified by mCDW. However, the temporal pattern agrees with simpler methods based on isotherm depths. We choose to present AD_{mCDW} since isotherm based metrics were found to be sensitive to the choice of isotherm. All code and additional details (including methods of determining end member water mass characteristics) are available in "Figure1.ipynb" of the provided jupyter binder environment.

Text S2.

Here we describe how estimates of α, F_{surf}, and Ψ_{in} are diagnosed from WAIS 1080 output. Further details and interactive code generating these values and associated figures may be found in "Supplementary_2.ipynb".

Ice-shelf melt coefficient: α

In our idealized model, we parameterize the 2D transport of buoyancy (units m³ s⁻³) from the ice shelf cavity into the upper, thermocline box due to ice shelf melt as

$$h(vb)_{in} = \alpha\, h_{mCDW}\, \Delta b_{melt}. \tag{2}$$

Using WAIS 1080 output, this 2D transport of buoyancy into the ocean thermocline box can be diagnosed as the total buoyancy transport to the ocean from basal ice shelf melt

(m^4 s^{-3}) divided by the idealized model width (m),

$$h(vb)_{\text{in}} = \frac{1}{L_x} \int_A F_{\text{iceshelf}} \, dA. \tag{3}$$

Here L_x (m) is the model zonal extent, F_{iceshelf} (m^2 s^{-3}) is the simulated buoyancy flux from the ice shelf to the ocean within the ice shelf cavity at each horizontal grid point on the ice shelf draft, and A is horizontal area of the ice shelf cavity (white box in Figure S1). Combining Ficeshelf1 and Ficeshelf2, we estimate the value of the parameter α as,

$$\alpha = \frac{1}{L_x \, h_{\text{mCDW}} \, \Delta b_{\text{melt}}} \int_A F_{\text{iceshelf}} \, dA \tag{4}$$

where $L_x = 55$ km and $\Delta b_{\text{melt}} = 6.7 \times 10^{-3}$ m s^{-2} (as described in the main text), while h_{mCDW} and the integrated buoyancy flux term are diagnosed from WAIS 1080.

The buoyancy flux F_{iceshelf} (m^2 s^{-3}) is defined functionally as (positive values increase the ocean buoyancy),

$$F_{\text{iceshelf}} = \frac{g\alpha_0}{\rho_{surf} c_p} Q_{H,\text{ice}} - g\beta_0 S_{surf} Q_{FW,\text{ice}} \tag{5}$$

where $g = 9.8$ m s^{-2} (gravity), $\alpha_0 = 4.8 \times 10^{-5}$ K^{-1} (thermal expansion coefficient), $\beta_0 = 7.8 \times 10^{-4}$ (haline contraction coefficient), $c_p = 3992$ J kg^{-1} K^{-1} (specific heat capacity of seawater), $\rho_{surf} = 1026$ kg m^{-3} (approximate surface cell density), $S_{surf} = 34$ (approximate surface cell salinity), $Q_{H,\text{ice}} = $ net heat flux from the ice (positive increases θ) (WAIS 1080 output), and $Q_{FW,\text{ice}} = $ net freshwater flux from the ice (positive increases S) (WAIS 1080 output). Figure S1 shows time mean WAIS 1080 F_{iceshelf} values for ice shelves in the Amundsen Sea Embayment and delineates (white box) the Dotson Ice Shelf horizontal region integrated over in alpha. Whilst the adjacent Dotson and Crosson ice shelves are connected in WAIS 1080, there is negligible flow between them across the

eastern boundary of the delineated region. The mCDW layer thickness, h_{mCDW} (m), is approximated as the thickness below the 0°C thermocline, computed from temperature spatially averaged over the ice front region (red box in Figure S1). Figure S2 shows h_{mCDW} directly diagnosed from WAIS 1080 and approximated from the ice shelf buoyancy input via alpha with $\alpha = 0.0021$ (mean diagnosed value).

Polynya surface buoyancy flux: F_{surf}

The ocean surface buoyancy flux, F_{surf} (m^2 s^{-3}), is defined functionally as (positive values increase the buoyancy of the surface cell),

$$F_{surf} = \frac{g\alpha_0}{\rho_{surf}c_p}Q_{H,\mathrm{oce}} - g\beta_0 S_{surf}Q_{FW,\mathrm{oce}}, \tag{6}$$

where $Q_{H,\mathrm{oce}}$ = net surface heat flux (positive increases θ) (WAIS 1080 output), $Q_{FW,\mathrm{oce}}$ = net surface freshwater flux (positive reduces S) (WAIS 1080 output), and all other parameters are as in Ficeshelf. To generate monthly and climatological mean timeseries of F_{surf}, which provides forcing to the idealized model (Figure S3), F_{surf} is averaged over a 55 km × 50 km region at the ice front where negative F_{surf} values are concentrated. This region is delineated in Figure S2 (red box). Our results are not qualitatively sensitive to the exact size of this region, and these values are simply intended to guide the magnitude of forcing terms.

In the main text we refer to F_{surf} as the surface buoyancy flux associated with net sea-ice formation. As defined in Fsurf, F_{surf} is the total surface buoyancy flux, not purely the buoyancy flux associated with sea-ice formation and melt. However, F_{surf} is tightly anti-correlated ($R^2 = 0.96, p = 10^{-240}$, Figure S3) with monthly net sea-ice formation in WAIS 1080 and so, for clarity, we refer to F_{surf} as reflecting sea-ice formation.

Cross-shelf volume transport: Ψ_{in}

Ψ_{in} (units m^2 s^{-1}) represents the net baroclinic shoreward transport of warm mCDW into the coastal region at the Dotson Ice Shelf front and the balanced offshore transport of cool thermocline waters. This term is estimated via a preliminary analysis of the Dotson Ice Front overturning circulation as simulated in WAIS 1080. We bin monthly mean volume transports across the edges of the ice front region (red box in Figure S1), and the corresponding monthly mean ocean temperature values, into surface referenced potential density (σ_0) bins using monthly mean σ_0 values. Density-binned volume transports into the ice front domain are then summed along the bounds of the box, whilst density-binned temperatures are averaged along the bounds of the box. When cumulatively integrated through σ_0 space, binned transports reveal a net shoreward flow of dense waters (interpreted as mCDW) and a net offshore flow of lighter waters (WW, glacial meltwater, and other surface waters), consistent with the assumptions of the model.

Text S2.

Analytical steady state solutions to the ice front overturning model

Analytical steady state solutions for the thickness of the thermocline layer and the thermocline stratification strengh in the ice front overturning model may be derived for known values of κ_{P},

$$h_{\mathrm{steady}} = \left(\frac{H}{2} - \frac{\Psi_{\mathrm{in}}}{2\alpha}\right) + \sqrt{\left(\frac{H}{2} - \frac{\Psi_{\mathrm{in}}}{2\alpha}\right)^2 + \frac{\kappa_{\mathrm{P}} L}{\alpha}} \tag{7}$$

$$\Delta b_{\mathrm{steady}} = \frac{\left(h_{\mathrm{steady}} - \frac{\Psi_{\mathrm{in}}}{\alpha}\right)\left(\frac{F_{\mathrm{surf}} L}{2\Psi_{\mathrm{in}}} + \Delta b_{\mathrm{melt}}\right)}{\frac{\kappa_{\mathrm{P}} L}{2\Psi_{\mathrm{in}}} + \frac{H}{2} - \frac{\Psi_{\mathrm{in}}}{\alpha}} - \Delta b_{\mathrm{melt}}. \tag{8}$$

May 26, 2023, 10:48pm

Interpretation of these solutions is complicated by the Δb dependence of κ_{P} (see equation (10) of the main text). To understand (7) and (8) in light of this dependence, consider the extreme case of taking $\phi \rightarrow \infty$ in equation (10) of the main text , which reverts κ_{P} to a step function transitioning from κ_{diff} to κ_{conv} when Δb drops below Δb_{crit}. In this case, (7) and (8) suggest two steady states for a given system $(H, L, \alpha, \Delta b_{\mathrm{melt}})$ and forcing $(\Psi_{\mathrm{in}}, F_{\mathrm{surf}})$; a diffusive steady state with $\kappa_{\mathrm{P}} = \kappa_{\mathrm{diff}}$ and a convective steady states with $\kappa_{\mathrm{P}} = \kappa_{\mathrm{conv}}$. In some regions of the forcing space, one of these κ_{P} values present a contradiction. Either setting $\kappa_{\mathrm{P}} = \kappa_{\mathrm{diff}}$ will result in $\Delta b_{\mathrm{steady}} < \Delta b_{\mathrm{crit}}$ (indicating the diffusive solution is not sustained, white regions in Figure 3b,c of the main text) or setting $\kappa_{\mathrm{P}} = \kappa_{\mathrm{conv}}$ results in $\Delta b_{\mathrm{steady}} > \Delta b_{\mathrm{crit}}$ (indicating the convective solution is not sustained, white regions in Figure 3d,e of the main text). Where neither κ_{P} value returns a contradiction, bistability is possible (region bound by yellow contour in Figure 3b-e of the main text). Smoothing the transition between κ_{diff} and κ_{conv}, by decreasing the value of ϕ, primarily acts to constrict the region over which bistability is possible. Numerical solutions presented in Figure 3 of the main text agree with analytical solutions (central panels of Figure S4), though they differ in that the numerical bistable region is contracted relative to the analytical bistable region, as anticipated for nonzero values of ϕ.

Summary of parameter sensitivity

These analytical solutions provide a fast and convenient means of exploring the sensitivity of model output to parameter choices. "Supplementary_3.ipynb" in the provided jupyter binder environment generates analytical versions of Figure 3 (main text) for the full suite of possible cases wherein each model parameter is both positively and negatively perturbed. Figure S4 illustrates the model steady state sensitivity to changes in α as an

May 26, 2023, 10:48pm

example; all other cases are available in the provided notebook. Table S1 summarizes the effects of varying each parameter, both on the analytical steady state solutions (explored in the jupyter notebok) and on transiently forced simulations (not shown). The positive feedbacks and related bistablity underpinning our main results depend on their being a nonlinearity to the dependence of vertical mixing on stratification strength. Within the confines of our choice to represent vertical mixing as a smoothed step function of stratification strength, we find that parameter perturbations can change the absolute magnitude of the thermocline depths associated with diffusive and convective conditions, can alter the length of the simulated lag between thermocline depth and stratification strength changes during regime transitions, and can change the strength of forcing perturbation required to trigger a regime transition. Small perturbations to the parameter values used in this study do not alter our key results, however, removing the jump in vertical mixing strength at the onset of convection does remove the described behavior.

References

Kim, T.-W., Yang, H. W., Dutrieux, P., Wåhlin, A. K., Jenkins, A., Kim, Y. G., . . . Cho, Y.-K. (2021). Interannual Variation of Modified Circumpolar Deep Water in the Dotson-Getz Trough, West Antarctica. *Journal of Geophysical Research: Oceans*, *126*(12), e2021JC017491.

Simpson, J., Allen, C., & Morris, N. (1978). Fronts on the continental shelf. *Journal of Geophysical Research: Oceans*, *83*(C9), 4607–4614.

Venables, H. J., & Meredith, M. P. (2014). Feedbacks between ice cover, ocean stratification, and heat content in ryder bay, western antarctic peninsula. *Journal of Geophysical Research: Oceans*, *119*(8), 5323–5336.
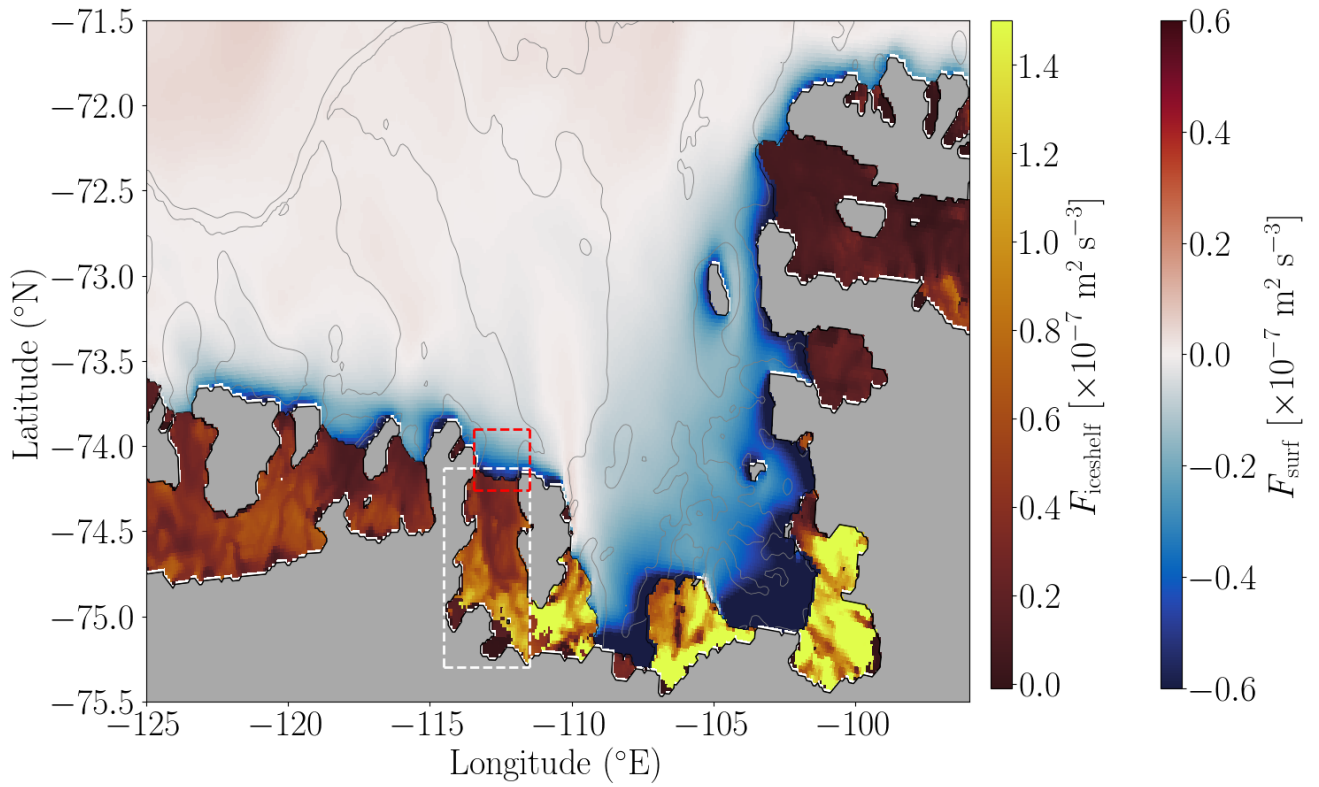
Figure S1. Time mean F_{iceshelf} and F_{surf} values from WAIS 1080 diagnosed according to equations Ficeshelf and Fsurf. F_{iceshelf} is defined for regions with positive ice shelf draft and F_{surf} is defined for regions of open ocean (zero ice shelf draft). The grounded ice zone is delineated with grey shading. Grey contours in the open ocean indicate bathymetry (500 m, 1000 m, 4000 m). The white dashed box indicates the region over which F_{iceshelf} is computed (the Dotson Ice Shelf) and the red dashed box indicates the region over which F_{surf}, Ψ_{in}, and h_{mCDW} are computed (the Dotson Ice Front).

May 26, 2023, 10:48pm

:
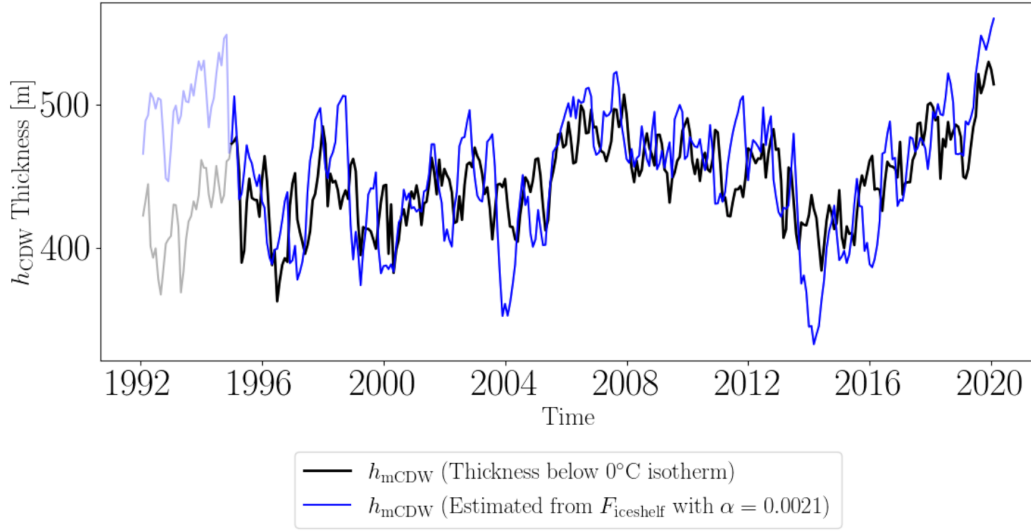
Figure S2. Timeseries of h_{mCDW} defined as either the thickness below the 0°C isotherm determined from monthly WAIS 1080 temperature output spatially averaged over the ice front region (black), or a linear function of spatially integrated Dotson Ice Shelf buoyancy fluxes (see equation Ficeshelf) with α set to 0.0021 (blue). The first three years (translucent lines) show worse agreement between the direct and parameterized h_{mCDW} values, possibly a result of model spinup.
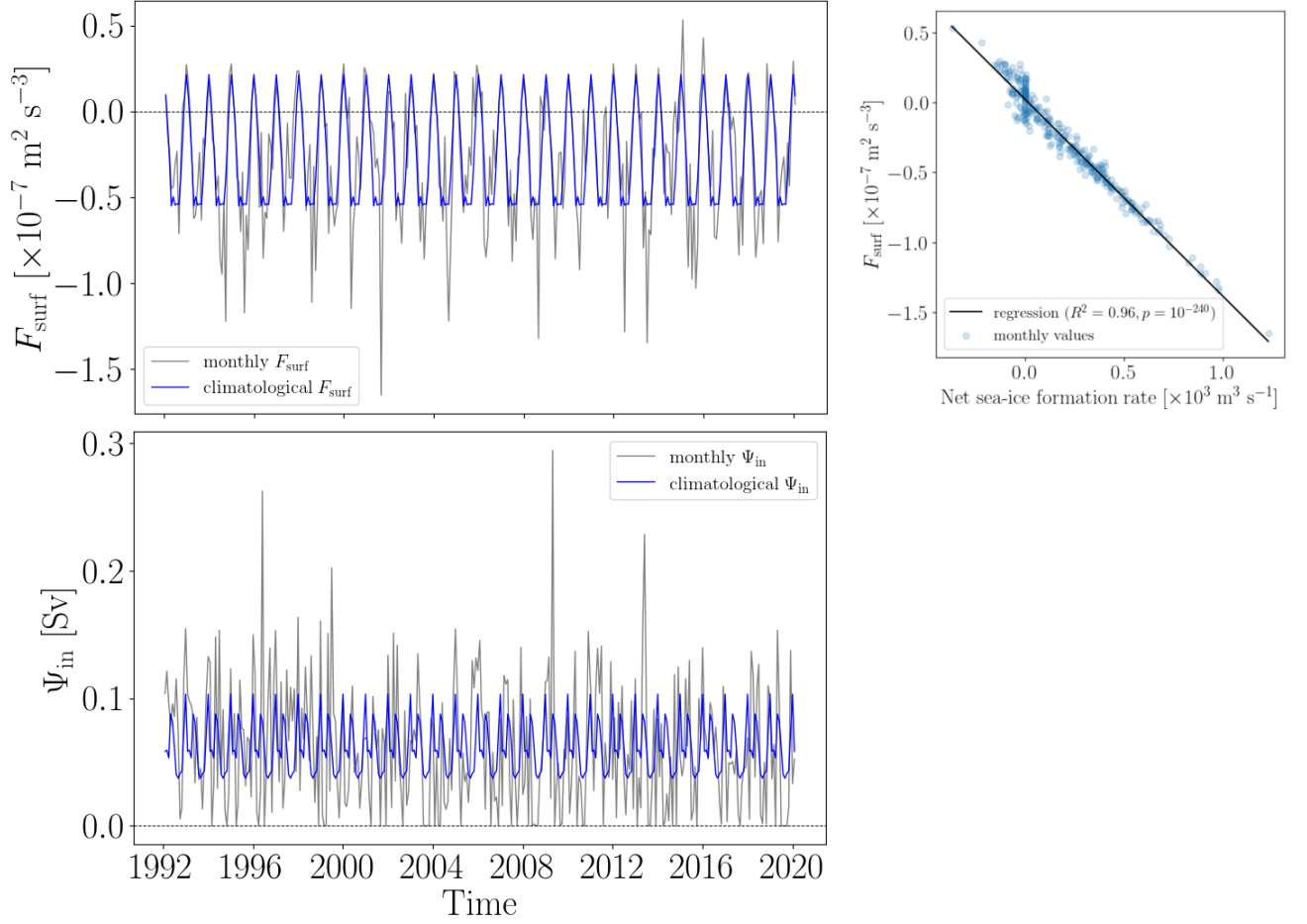
Figure S3. Monthly mean values (grey) and climatological mean monthly values (blue) of F_{surf} (upper) and Ψ_{in} (lower) as diagnosed from WAIS 1080. (right) Correlation between F_{surf} and monthly net sea-ice formation rates in the Dotson ice front region.
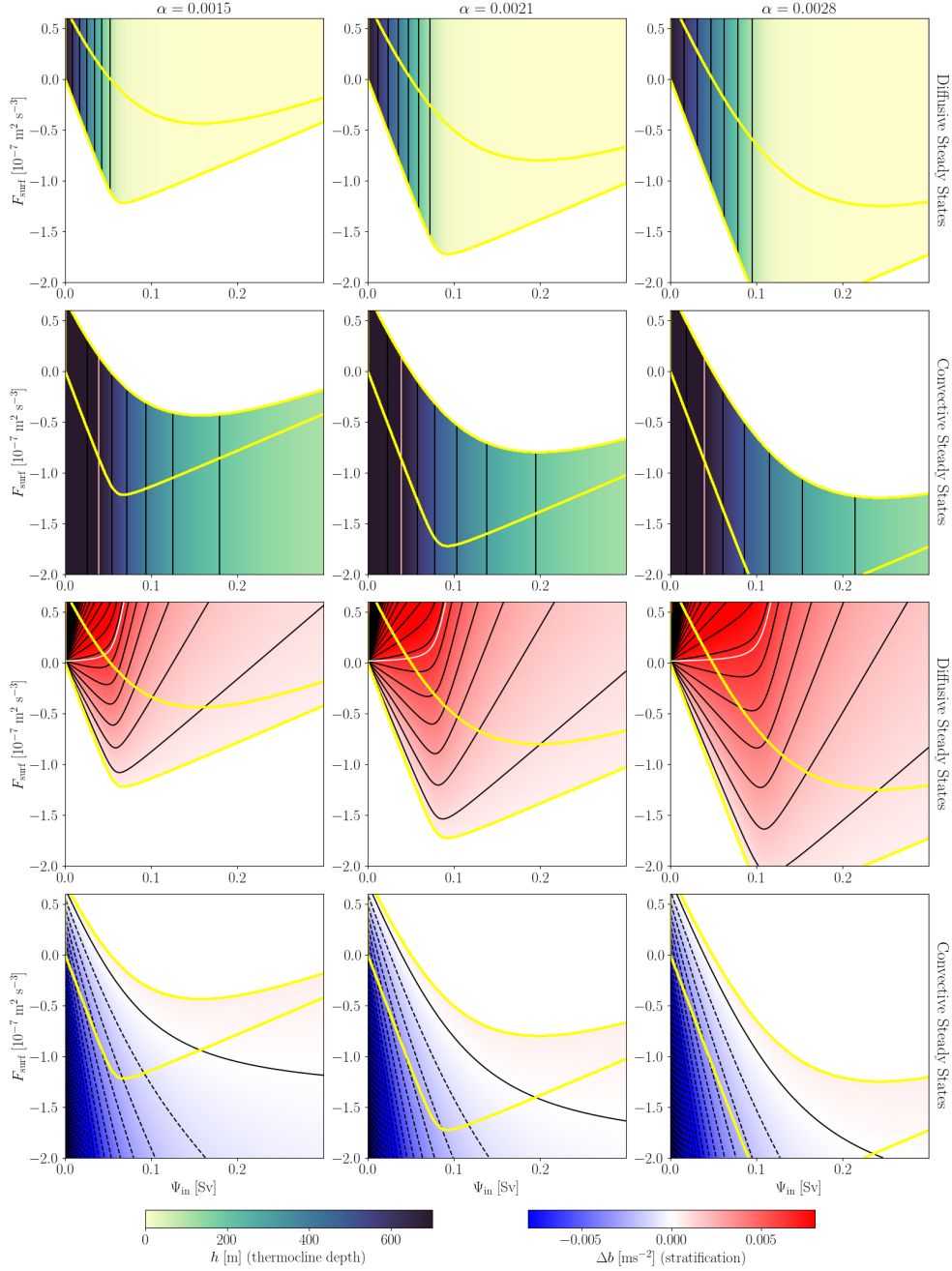
Figure S4. Illustration of the sensitivity of analytical steady-state solutions to perturbations of the parameter α. Each column contains panels equivalent to Figure 3b-e of the main text, except analytical solutions rather than numerically equilibrated solutions are shown. The central column shows analytical steady-state solutions to our model when the default (main text) parameter values are used (these panels may be directly compared to Figure 3b-e). Columns to the left and right show analytical steady-state solutions when α is reduced and increased, respectively.
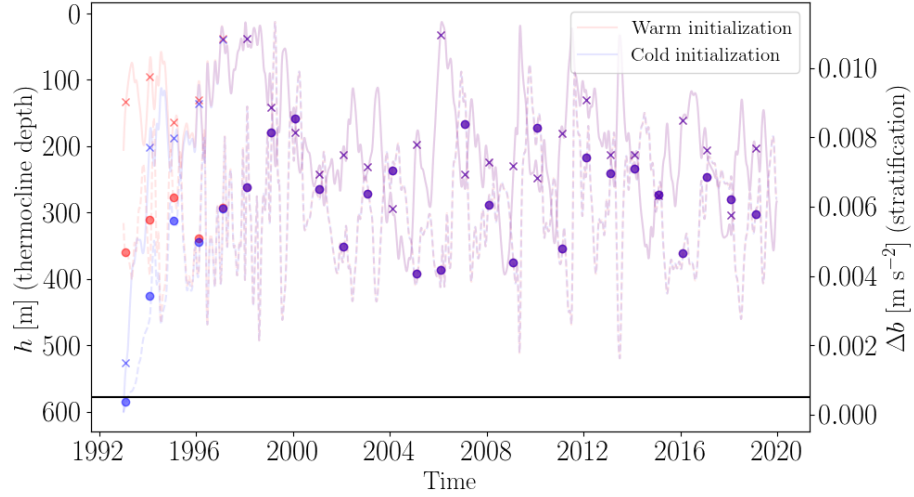
Figure S5. Thermocline depth changes and stratification strength changes simulated in response to monthly (as opposed to climatological) WAIS 1080 forcing. The same forcing is applied to the model initialized in warm conditions (red) and cold conditions (blue). Crosses, circles, solid lines, and dashed lines are as in Figure S6. Black horizontal line is Δb_{crit}, stratification strength does not drop below this value following initialization.
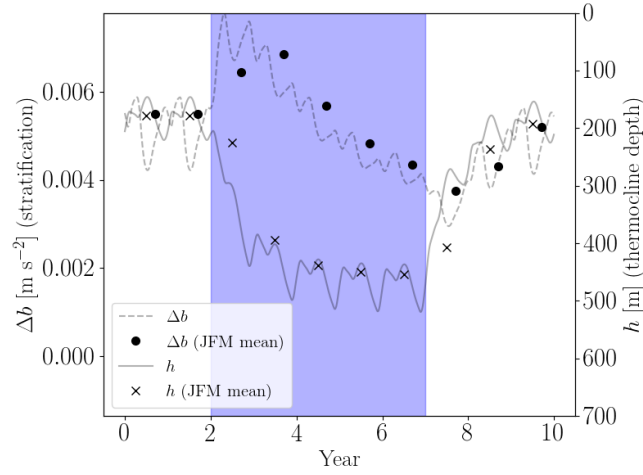
Figure S6.   Similar to Figure 4d for the main text. In Figure 4d, winter (May-September) Ψ_{in} values are shifted downwards for two consecutive years. Here the full annual pattern of Ψ_{in} is downshifted (by the same amount as in Figure 4d, the maximum offset that ensures $\Psi_{\text{in}} > 0$) for 5 consecutive years. Whilst this forcing pattern generates large decadal scale fluctuations in the thermocline depth, it does not trigger regime change as the accompanying stratification changes do not promote the onset of convection.

Table S1. Dominant effects of increasing the magnitude of a parameter on the analytical steady state solutions to the ice front overturning model and the implied effect on transiently forced solutions. Effects of decreasing parameter magnitudes are the converse in all cases.

Parameter	Effect (analytical steady state)	Implied Effect (transient)
α	α dictates the sensitivity of meltwater generation to the thickness of the ice front mCDW layer. Increasing α acts to: - strengthen the ice front stratification associated with a given thermocline depth - deepen the steady state thermocline associated with a given mCDW inflow - shift the bistable region towards negative F_{surf} values (see Figure S3.1)	Stronger perturbations are needed to force diffusive to convective transitions and weaker perturbations are sufficient to force convective to diffusive transitions. Both convective and diffusive solutions are associated with deeper thermoclines.
Δb_{melt}	Δb_{melt} similarly dictates the sensitivity of ice front stratification strength to basal ice melt. It has a similar effect to α except it only influences steady state stratification strengths, not steady state thermocline depths.	Same as α, except does not effect end member thermocline depths.
κ_{diff}	κ_{diff} only effects diffusive end member solutions and increasing it acts to: - deepen the steady state thermocline associated with diffusive end members - contract the bistable region from below such that diffusive solutions are not supported for a wider range of negative F_{surf} values (when $\kappa_{\text{diff}} = \kappa_{\text{conv}}$ bistability disappears altogether as the end member solutions converge)	Diffusive solutions are associated with deeper thermoclines generally and transitions to convective solutions are possible with weaker perturbations.
κ_{conv}	κ_{conv} only effects convective end member solutions and increasing it acts to: - deepen the steady state thermocline associated with convective end members - expand the bistable region from above such that convective solutions are supported for a wider range of positive F_{surf} values (when κ_{diff} and κ_{conv} become more similar bistability contracts, when κ_{diff} and κ_{conv} become more different bistability expands)	Convective solutions are associated with deeper thermoclines generally and transitions to diffusive solutions require stronger perturbations.
Δb_{crit}	Simply changes the stratification strength at which convection onsets. Increasing Δb_{crit} will shift the bistable region towards positive F_{surf} values.	Stronger perturbations are needed to force convective to diffusive transitions and weaker perturbations are sufficient to force diffusive to convective transitions.
ϕ^a	Increasing ϕ makes κ_{P} more step-like, therefore bringing the numerical model behavior closer to the analytical solution. Decreasing ϕ, by contrast, smooths out κ_{P}. This renders more solutions with steady state stratification strength close to the critical buoyancy unstable, and thus contracts the bistable region.	Transitions will require greater perturbations when ϕ is larger.

[a] analytical solutions are independent of ϕ, its effect has been assessed using numerical solutions